applied sciences

MDPI

Article

Influence of Interference Fit and Temperature on High-Speed Permanent Magnet Motor

Yiming Zeng, Shanju Yang *, Xinyi Yang, Qi Wang, Lijun Zhang, Jie Hao and Wencan Hua

College of Mechanical and Electronic Engineering, Northwest A&F University, Yangling 712100, China; 2022051012@nwafu.edu.cn (Y.Z.); 15909161734@163.com (X.Y.); wcbqwangqi@nwafu.edu.cn (Q.W.); zljlxm@nwsuaf.edu.cn (L.Z.); haojienwafu@163.com (J.H.); huawencan@nwafu.edu.cn (W.H.)
* Correspondence: yangshanju@nwafu.edu.cn

Abstract: A high-speed permanent magnet motor is the core driving component of a centrifugal air compressor. The power of the centrifugal air compressor is output by the motor. Its safety and reliability are embodied in the stability of the rotor structure, which greatly affects the stability and working efficiency of the centrifugal air compressor. Much research has focused on the material strength, structural characteristics, and fit clearance of a high-speed rotor, whereas few research articles have focused on the influence of interference fit of high-speed and ultra-high-speed permanent magnet motors, and there is also little research on the thermal failure caused by temperature in high-speed motors. In this paper, the influence of the interference fit and temperature of the high-speed permanent magnet motor is studied. Using finite element analysis conducted by Ansys to obtain simulation data, the influencing factors of the strength of the interference are analyzed comprehensively in the centrifugal compressor rotor system. The interference value and rotational speed range are determined via numerical calculation. Under the condition of minimum interference, when the calculated speed reaches 137,628.82 rpm, the structure of the rotor is loose and fails, which is a mechanical failure caused by the relative sliding of the magnet and the sheath. The calculated speed value differs from the simulation result by about 1.2%. The simulation results show that the maximum stress of the structure can be reduced from 1186.1 MPa to 308.42 MPa by adding chamfer to the end covers in interference fit structure. The effects of interference value, rotational speed, temperature, and sheath thickness on the structure are also analyzed. From the perspective of temperature on structural reliability, the failure temperature of the structure decreases when the interference value increases. The lowest failure temperature is 182.3 °C when the interference value is 70 μm. After that, the interference value increases and the failure temperature increases. The reason for this is the interaction between radial stress and contact stress. These results are caused by the interaction between interference fit and temperature, which should be paid attention to when the structure of a high-speed permanent magnet motor is designed.

Keywords: rotor strength; chamfer; finite element analysis; interference fit; stress; failure temperature

check for updates

Citation: Zeng, Y.; Yang, S.; Yang, X.; Wang, Q.; Zhang, L.; Hao, J.; Hua, W. Influence of Interference Fit and Temperature on High-Speed Permanent Magnet Motor. *Appl. Sci.* **2023**, *13*, 11331. https://doi.org/10.3390/app132011331

Academic Editor: Frede Blaabjerg

Received: 5 September 2023
Revised: 26 September 2023
Accepted: 2 October 2023
Published: 16 October 2023

Copyright: © 2023 by the authors. Licensee MDPI, Basel, Switzerland. This article is an open access article distributed under the terms and conditions of the Creative Commons Attribution (CC BY) license (https://creativecommons.org/licenses/by/4.0/).

1. Introduction

A high-speed permanent magnet motor has a sound momentum of growth [1], and its application areas involve aerospace [2,3], new energy vehicles, high-speed turbomachinery, industrial machinery [4], intelligent agriculture [5], etc. This is due to their small size and light weight while achieving high-density power and the maximum satisfaction of working conditions [6,7]. The development of a high-speed permanent magnet motor follows the trend of lightweight technology. The application area will be fully popular and covered in the future when the technology becomes more mature [8].

In motors, the compressive strength of permanent magnets is much greater than the tensile strength; therefore, permanent magnets and alloy steel sheath are generally assembled by interference fit [9]. In the interference fit, the interference value is one of

the key factors that affects the rotation of the high-speed motor [10]. If the interference value is too large, the magnet will collapse. In the process of high-speed rotation, the actual interference value is less than the static value. If the interference value is too small, it will easily cause the sheath to fall off. On the one hand, the magnet cannot be protected; on the other hand, it will cause the safety problem of falling off and splashing [11].

A high-speed permanent magnet motor is the core driving component of a centrifugal air compressor. The power of the centrifugal air compressor is output by the motor. Energy conversion is transmitted to the impeller through the motor. Its safety and reliability are embodied in the stability of the rotor structure, which greatly affects the stability and working efficiency of the centrifugal air compressor. This paper focuses on the rotor system of aero-dynamic bearing in the centrifugal compressor. Through simulation, the stress of the magnet and sheath of a high-speed permanent magnet motor under the interference fit is explored, and the factors of rotor strength are analyzed [12–14].

Gan et al. [15] analyzed the critical speed, unbalance response, and stability of the shaft system in detail, and they proposed an investigation scheme of the rotor strength and rotor dynamic characteristics for high-speed and high power switched reluctance machines (SRMs). On the basis of rotor strength constraint, Xu et al. [16] presented the composite sheath of a high-speed permanent magnet generator to make the stress distribution reasonable and reduce eddy current loss. Shao et al. [17] analyzed the influences of static interference and the thickness of sleeve and sleeve material on the rotor strength and summarized the strength design rules of an ultra-high-speed permanent magnet synchronous rotor. A lot of research mainly focuses on the influence of parameters, and research on the variation in the interference structure is insufficient. According to the simulation results of stress, we adopt a method which adds chamfer to the end covers of the magnet to reduce the maximum principal stress. This method can reduce the probability of permanent magnet collapse.

The heating condition of an ordinary motor may be relatively low, but the heating condition of a high-speed motor is serious due to the higher speed and greater power. The temperature has a great impact on the stability of a high-speed motor [18–20]. It is valuable to focus on the relationship between temperature and rotor strength of a high-speed motor. It has been found that most studies focusing on the rotor strength of the interference fit and temperature only analyze the relationship between stress and temperature under one simple interference condition. Chen et al. [21] simplified the rotor stress condition as a plane stress problem, and the analytical formulae for rotor strength was proposed based on the displacement method in polar coordinates to accurately predict the stress and displacement of the motor rotor with a high speed and rising temperature. Du et al. [22] considered the non-isothermal distribution of rotor temperature, and 3D temperature–stress coupling analysis was performed to obtain the optimal sleeve thickness. Du et al. [23] proposed a multi-physical field optimization process for high-speed permanent magnet machines to achieve low loss and a low temperature. Gu et al. [24] focused on the thermal effect on mechanical strength and stiffness, and a reasonable machine design was proposed to achieve a more accurate mechanical distribution. The main purpose of these studies is to illustrate the effect of temperature on the structure and to reduce the temperature through design optimization.

However, there are few studies which focus on structural failure due to temperature. In this paper, the focus of temperature research is mainly to analyze the failure temperature of interference fit structure based on a variable interference value, not only limited to one condition, and uniform sampling in the range of permitted overfill for the analysis of failure.

2. Materials and Methods

As shown in Figure 1, the high-speed motor rotation system is mainly composed of the stage impellers, the spindle, the fixed nuts, and so on. Thereinto, the spindle consists of the sheath, the end covers, and the magnet, which constitutes the interference fit structure.

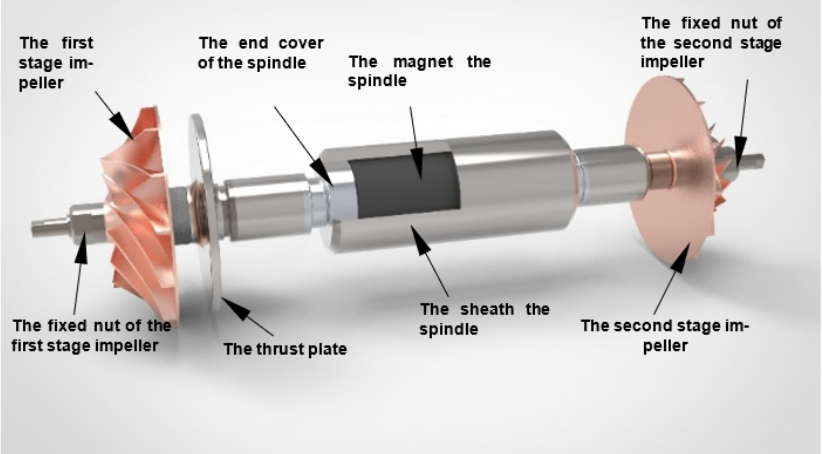


Figure 1. The rotor system structure of the centrifugal compressor.

The interference fit is adopted between the sheath and the rest of the spindle, in which the contact position between the sheath and the end cover is welded, as shown in Figure 2.

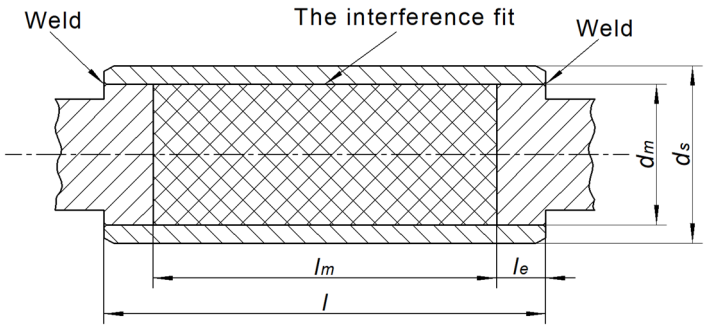


Figure 2. Structural diagram of the rotor system.

The diameter of the magnet d_m is 28.5 mm and the shaft length l_m is 70 mm. The outer diameter of the sheath d_s is 36 mm and the shaft length of the sheath l is 90 mm. The length of the end cover and the part of the interference fit of the sheath l_e is 10 mm.

The materials and physical properties of the magnets, sheath, and end covers are shown in Table 1 below.

Table 1. Material performance parameters of interference fit components.

Parts	Magnet	Sheath	End Covers
Materials	Sm2Co17 magnet	Stainless steel 3Cr13	Stainless steel 3Cr13
Density(kg/m^3)	8400	7750	7750
Poisson's ratio	0.24	0.28	0.28
Modulus of elasticity (GPa)	117	206	206
Compressive yield strength (GPa)	509	540	540
Tensile yield strength (MPa)	35	540	540

2.1. Calculation of the Static Minimum Interference

The minimum interference should satisfy the requirement when the motor works at the maximum torque M; the coordination of the magnet and the sheath will not slip and rotate. Therefore, the formula of minimum binding pressure can be obtained [25]:

$$P_{\min} \geq \frac{2M}{\pi {d_m}^2 f l} \tag{1}$$

where d_m is the fit diameter, that is, the diameter of the magnet and the inner diameter of the sheath, mm; f is the friction coefficient of the mating surface, 0.2; and l is the mating length, mm.

The minimum amount of interference is:

$$\delta_{\min} = P_{\min} d_m \left(\frac{C_m}{E_m} + \frac{C_s}{E_s} \right) \tag{2}$$

where C_m and C_s are the stiffness coefficients of the magnet and the sheath, respectively, and they are expressed as follows:

$$C_m = \frac{{d_m}^2 + {d_{om}}^2}{{d_m}^2 - {d_{om}}^2} - v_m \tag{3}$$

$$C_s = \frac{{d_m}^2 + {d_s}^2}{{d_s}^2 - {d_m}^2} + v_s \tag{4}$$

where v_m and v_s are the Poisson's ratio of the magnet and sheath; d_{om} and d_s are the outer diameters of the magnet and sheath, and $d_{om} = 0$; E_m and E_s are the elastic modulus of the magnet and sheath.

The minimum interference $\delta_{\min}$ between the magnet and sheath can be obtained by Formulas (1) and (2).

2.2. Calculation of the Maximum Interference

The design of the maximum interference should be ensured so that the interference can fit the parts of the magnets, end covers, and sheath. In addition, plastic deformation will not be produced. As obtained from Table 1, the yield strength of stainless steel σ_{ss} is greater than that of magnetic sticks σ_{sm}. Therefore, the maximum pressure of the magnet without plastic deformation $P_{\max}$ is as follows:

$$P_{\max} = \alpha \sigma_{sm} \tag{5}$$

where $\alpha = \frac{1-q_a^2}{\sqrt{3+q_a^4}}$ and $q_a = \frac{d_m}{d_s}$.

Finally, the maximum interference $\delta_{\max}$ can be obtained by bringing in the maximum pressure (2).

2.3. Calculation of Dynamic Loss of Interference

In the process of the high-speed operation of the motor, both the magnet sheath and the magnet are affected by the centrifugal force. The inner diameter of the sheath and the diameter of the magnet become larger. However, for the sheath there is a thin-walled part, and the stiffness is less than that of the magnet; the increase in the inner diameter of the sheath will be higher than the diameter of the magnet. Therefore, when the motor rotates, the actual interference is less than the static interference. Based on this phenomenon, the amount of interference lost δ_ω should be calculated to avoid failure.

Under the condition of high rotation, the formula for calculating the radial displacement δ_m of the diameter of the magnet is as follows [9]:

$$\delta_m = \frac{2\rho_m\omega^2(1-v_m)}{4gE_m}\cdot\left(\frac{d_m}{2}\right)^3\cdot 10^{-5} \tag{6}$$

where ρ_m is the density of the magnet, kg·m^{-3}, and ω is the angular speed of the motor.

Under the condition of high rotation, the formula for calculating the radial displacement δ_s of the inner diameter of the sheath is as follows:

$$\delta_s = \frac{2\rho_s\omega^2(1-v_s)(3+v_s)}{8gE_s}\cdot\left(\frac{d_m}{2}\right)^3\cdot\left(\frac{2}{1-v_s}+\frac{2}{3+v_s}\right)\cdot 10^{-5} \tag{7}$$

where ρ_s is the density of the magnet, kg·m^{-3}.

The loss of interference in the state of high-speed rotation δ_ω is as follows:

$$\delta_\omega = \delta_s - \delta_m \tag{8}$$

According to the above formulas, when the motor is running at high speed, it is necessary to ensure that the residual interference is still greater than the minimum interference $\delta_{\min}$. Comprehensively speaking, the designed amount of the interference Δ can be taken:

$$\Delta = k(\delta_{\min} + \delta_\omega) \tag{9}$$

For high-speed motors, k is generally 1.5–2. Its value is taken to be 2 in the calculation in order to leave a larger safety margin.

2.4. Calculation of Loose Speed

It can be obtained from Formulas (6) to (8) that the amount of the loss of interference δ_ω of the high-speed motor rises with the increase in the rotational speed. With the rotational speed increasing, the residual interference of the matching surface of the magnet and the sheath is less than the minimum effective interference $\delta_{\min}$. Slip and relative rotation will occur, and even serious consequences of separation and loosening might be caused. Therefore, in order to ensure the normal operation of the motor, the maximum speed that can be withstood under the designed interference should be calculated.

When $\Delta - \delta_\omega \geq \delta_{\min}$, slip does not occur, and the rotational speed is loosened at this time. Combined with Formulas (6)–(8), the rotational speed [9] n is calculated by:

$$n \leq \frac{30}{\pi}(\Delta-\delta_{\min})^{\frac{1}{2}}\left[\begin{array}{c}\frac{4\rho_s}{8gE_s}\cdot\left(\frac{d_s}{2}\right)^3(3+v_s+1-v_s)\\ -\frac{2\rho_m(1-v_m)}{4gE_m}\left(\frac{d_m}{2}\right)^3\end{array}\right]^{-\frac{1}{2}} \tag{10}$$

The diameter of the magnet is 28.5 mm, and the shaft length is 70 mm. The outer diameter of the sheath is 36 mm, and the shaft length of the sheath is 90 mm; the length of the interference fit between the end cover and the sheath is 10 mm; the motor rated power is 26 kW; and the speed is 30,000 to 100,000 rpm.

Combining the above conditions, the effective value range of the design interference is 3.04 to 85.28 μm, and the minimum design interference can bear the loose speed of 137,628.82 rpm.

The reliability of loose speed calculated by the empirical formula still needs to be verified. It is verified by simulation in this paper, which is described in detail below.

3. Static Strength Check of Interference Fit

Strength verification of the magnet–sheath interference fit is performed by using the static analysis module in the ANSYS Workbench [26]. To give the 3D model structure

and material properties, the simulation results are analyzed, and the key factors of rotor strength are investigated after the mesh division, boundary condition setting, and solution.

3.1. Finite Element Modeling

Finite element analysis (FEA) is a kind of engineering analysis technology based on numerical analysis. It is an effective method to solve various engineering problems effectively by using mathematics and computer technology. This method can effectively estimate the performance and reliability of the structure, determine the existence of factors in the production process, and optimize the design scheme.

The basic principle of FEA is to discretize the continuous solution domain into a combination of elements. Within each element, an assumed approximate function is used to piecewise represent the unknown field function to be solved on the solution domain. Typically, the approximate function is represented by the numerical interpolation functions of the unknown field function and its derivatives at the nodes of the element. Thus, a continuous infinite degree of freedom problem becomes a discrete finite degree of freedom problem.

In this paper, the interference fit of the rotor system originates from the high-speed motor module in the centrifugal compressor. The sheath and end cover are made of stainless steel 3Cr13, and the magnet is made of Sm_2Co_{17}. Using SolidWorks2021 modeling software (Dassault Systèmes SolidWorks Corporation, Waltham, MA, USA, https://www.solidworks.com/contact-us), the drawn model is imported into the static analysis module of ANSYS2021 Workbench (Ansys, Canonsburg, PA 15317 USA, https://www.ansys.com/contact-us), and the corresponding material properties and working temperature are set. After that, the contact conditions and mesh division are created for the structure. When the FEA simulation is only involved in the inherent elements of the rotor (i.e., the sheath, the end covers, and the magnet), which rotate at the same angular velocity to maintain their relative positions, the static mesh editor is used. Once the FEA simulation is not involved in the parts from the stator and gap, there is no need to use dynamic mesh. As shown in Figure 3, because the structure of the impellers is not axisymmetric, a 3D mesh model is used for the interference simulation. The results of the mesh sensitivity analysis are shown in Figure 4. When the number of elements reaches 120,000, the maximum stress value tends to be stable. It is obvious that the grid being divided into 120,739 can shorten the simulation time and ensure the accuracy of the results. Then, the parameters are set and solved.

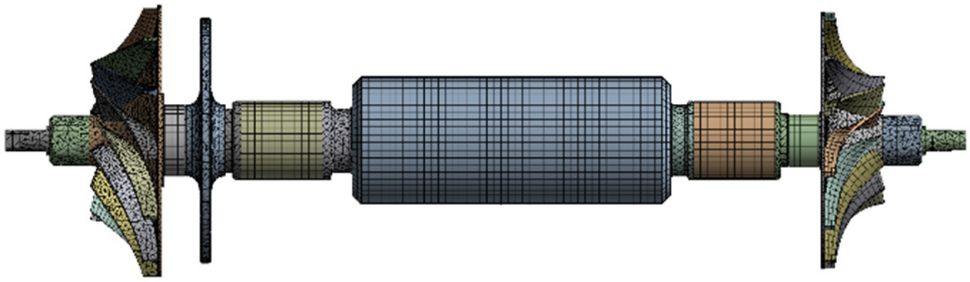


Figure 3. Meshing diagram of the rotor system.

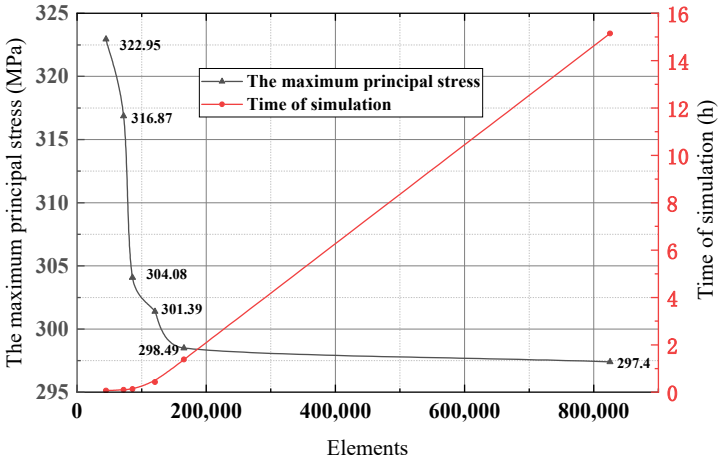


Figure 4. Results of the mesh sensitivity analysis of the model.

3.2. Verification of Loose Speed

The reliability of the loose speed obtained from the empirical formula is verified by taking the simulation method. Under the condition of a minimum design interference of 3.04 μm, the size of the rotational speed is changed, and the speed range of failure can be determined according to the simulation results. It is also significant whether the loose phenomenon occurs on the contact surface of the interference fit. As shown in Figure 5, when the rotational speed is 140,000 rpm, the contact surface of the interference fit is loose and slidable.

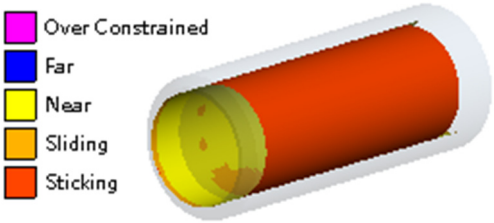


Figure 5. Interference fit contact surface state at 14,000 rpm.

When the rotational speed is 130,000 rpm and below, the simulation results are still valid. When the simulated speed ranges from 130,000 rpm to 140,000 rpm, the structure fails, and the failure speed is about 136,000 rpm. This is a mechanical failure caused by the relative sliding of the magnet and the sheath. However, the calculated result of the empirical formula is 137,628.82 rpm, and the error with the simulation result is about 1.2%. Therefore, the calculation results are reliable.

3.3. Analysis of Finite Element Simulation Results

The speed selected for the simulation is set according to the actual working needs. The rated speed under a normal working condition is 88,000 rpm, and the working temperature is 22 °C. The interference of the rotor system is taken as 60 μm. Stress, deformation, and elastic strain are added as the output results to analyze the strength condition of the rotor.

3.3.1. Result Analysis

As shown in Figure 6a–c, the maximum deformation is 35.33 μm; the maximum elastic strain is 0.00585; and the maximum principal stress is 1186.1 MPa in the interference fit region of the rotor system. As shown in Figure 6d, the maximum stress region which exceeds the permissible stress and where failure occurs is located at both ends of the magnet.

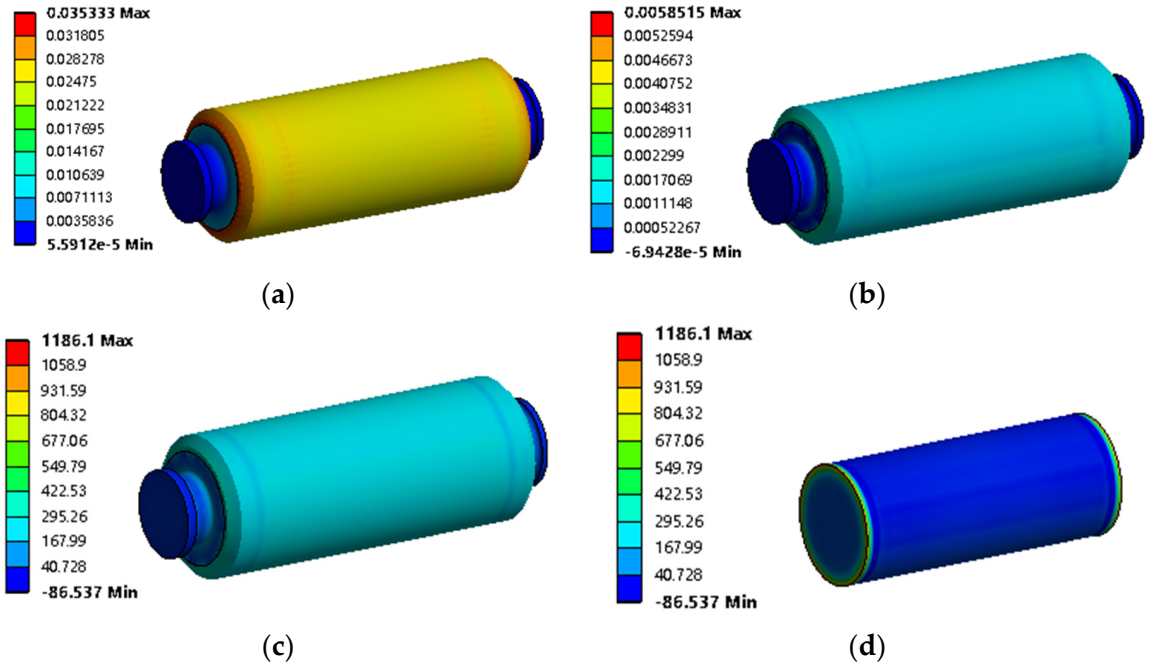


Figure 6. Distribution of simulation results surface. (**a**) Total deformation distribution; (**b**) elastic strain distribution; (**c**) total stress distribution; (**d**) stress distribution of the magnet.

3.3.2. Radial and Axial Stress Distribution

In order to accurately locate the specific location of the stress failure, the radial path stress change in the sheath magnet and the axial path stress change in the mating surface are added according to the above results of the output stress figure. As shown in Figure 7a,b, 200 nodes are sampled on the radial and axial paths, respectively.

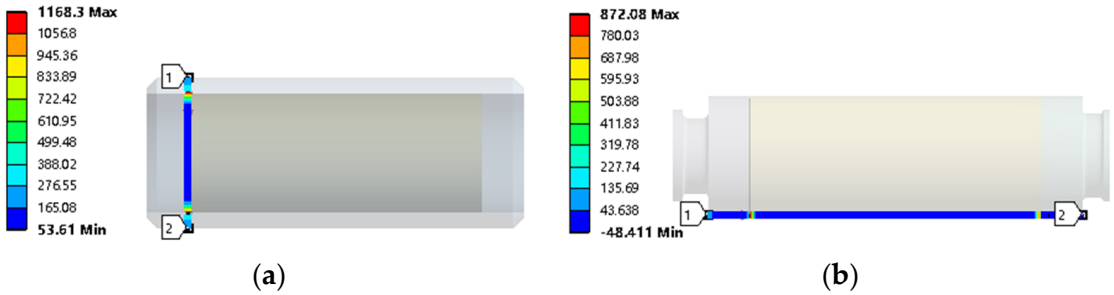
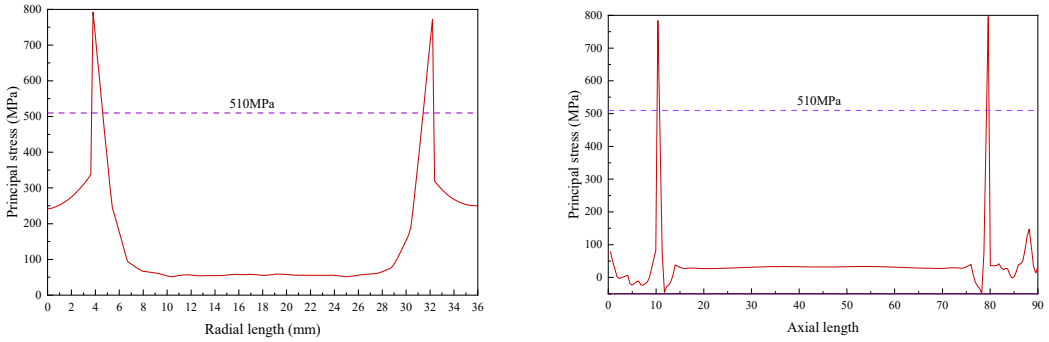


Figure 7. Axial and radial stress distribution. (**a**) Radial direction; (**b**) axial direction.

Observing the location of the specific failure in the interference fit as shown in Figure 8a,b, the radial and axial stresses are approximately symmetrical along their midpoints according to the results of the sampling nodes. There is an obvious stress mutation at the vertices where the sheath, magnet, and end covers are in contact. Comprehensive analysis shows that the end cover, magnet, and sheath squeeze each other in the interference fit. Great strain and deformation occur at both ends of the magnet cylinder, which is the contact edge effect of the interference fit that creates a stress concentration at the edge [27].



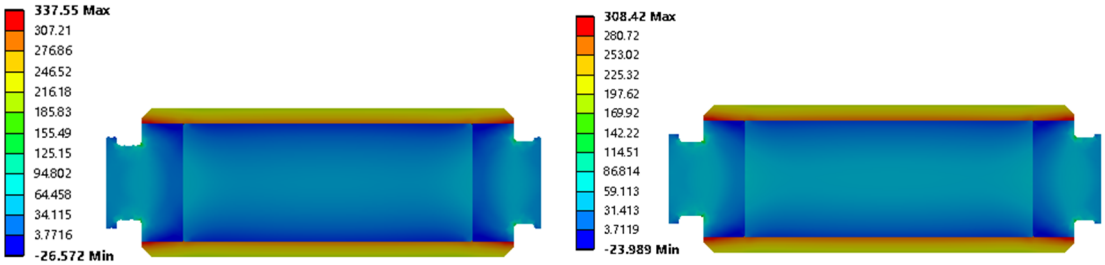
(**a**) (**b**)

Figure 8. The distribution of axial and radial stress curves. (**a**) Radial direction; (**b**) axial direction.

3.4. Measures to Reduce Maximum Stress

3.4.1. Chamfers Position of Interference Fit Structure

According to the structure of interference fit in the rotor system, two methods of cutting 45° chamfers, meaning that the top of both sides of the magnet and the top of the two end covers are added, respectively, are adopted. Comparing the two different structures under the condition of keeping the speed, temperature, and interference consistent above, to change the position of the chamfers, rebuild the model, and simulate, the result is the chart of stress distribution along the radial section, as shown in Figure 9. Setting the chamfers to 0.5 mm as an example, chamfers are added on the magnet and the end covers, respectively, to compare the parameter changes in them. The maximum principal stress on the sheath is 337.55 MPa and 308.42 MPa, respectively, which is significantly lower than the structure without chamfers, and the maximum stress is also within the range of allowable stress.



(**a**) (**b**)

Figure 9. Two kinds of structural stress distribution. (**a**) The magnet chamfered structure; (**b**) the end covers chamfered structure.

Based on the radial and axial stress distribution of the original structure, the stress distribution data of magnet chamfers and the end cover chamfer structure are added. As shown in Figure 10, a comparative diagram of stress distribution is drawn.

The simulation parameters of the three structures are compared and analyzed, as shown in Table 2. Under the normal working condition, there is little difference in the total deformation and elastic strain among the three structures. However, there is a great difference in the maximum principal stress between the original structure and the two chamfered structures. The maximum principal stress of the magnet chamfers structure and the end cover chamfers structure is on the sheath, and the maximum stress of the end cover chamfers structure is smaller than the former.

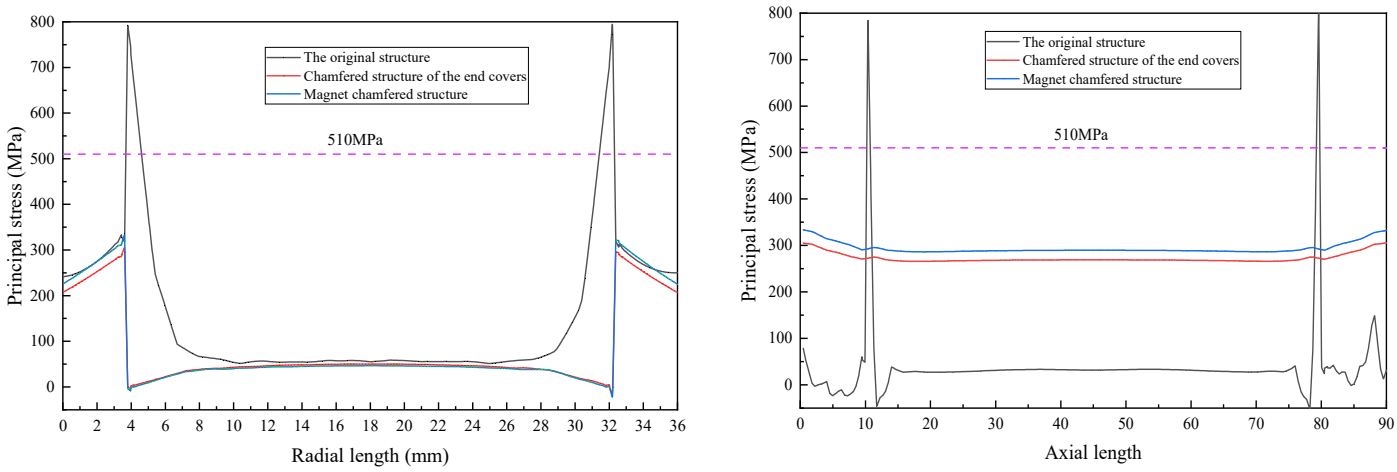


Figure 10. The comparison of axial and radial stress distribution of three structures. (**a**) Radial direction; (**b**) axial direction.

Table 2. The comparison of simulation parameters of three structures.

Parameters \ Structures	Total Deformation (mm)		Strain of Elasticity (mm/mm)		Principal Stress(MPa)	
	Min	Max	Min	Max	Min	Max
(a) The original structure	5.59×10^{-5}	0.0353	-6.94×10^{-5}	0.0059	−86.537	1186.10
(b) The magnet chamfered structure	1.94×10^{-5}	0.0300	-4.28×10^{-5}	0.0020	−26.572	337.55
(c) The end covers chamfered structure	3.78×10^{-5}	0.0275	-8.32×10^{-6}	0.0019	−23.989	308.42

Considering the processing factors, it is difficult to process the magnet because of its brittleness and easy-to-produce cracks at the top. Therefore, to choose the chamfered structure of the end cover, on the one hand, the material of the end cover is structural steel, which is convenient for processing; on the other hand, the maximum principal stress of the chamfered structure of the end cover is smaller.

3.4.2. Chamfers Size of the Interference Fit Structure

In conclusion, choosing to add chamfers at the end cover can reduce the maximum principle stress and prevent the problem of strength failure in the structure of the interference fit. According to this design, we make the simulations of the end cover chamfers range from approximately 0.3 to 1.0 mm in order to compare the effect of the size of the chamfers on the stress of the interference fit structure. The exploratory results are shown in Figure 11.

By increasing the end cover chamfers, the stress in the interference fit region shows a decreasing trend. When choosing the chamfer size, we should consider the size of the stress and the material and processing of the end cover so as to ensure that the maximum principal stress of the interference fit is small, and that it is easy to process and reduce the material loss.

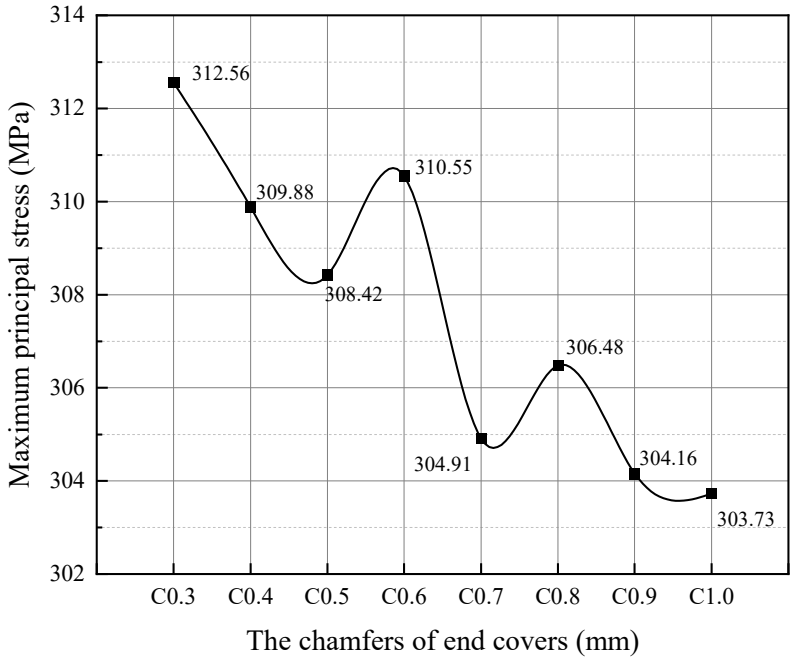


Figure 11. The stress distribution under different chamfered structures.

4. Results and Discussion

After changing the geometric structures, that is, adding a chamfered structure to the end covers, the local high stress of the interference fit can be greatly reduced. On this basis, we continue to explore the factors affecting the strength of the rotor. According to the degree of change in the strain, deformation, and stress, the change in stress is more significant than others, so the following is mainly through the change in stress to show the influence of various factors on the strength of the rotor.

4.1. Amount of Interference

The rated speed of the centrifugal compressor used in the experiment is 88,000 rpm, the highest speed is 96,000 rpm, and the maximum speed is increased by 16.7%, that is, 112,000 rpm.

For the rigor of the conclusion, the speed 60,000 rpm under the rated speed is compared with the former. The structure of end covers used in the simulation is C0.5 in order to analyze the stress and strain of the rotor system at different speeds.

Within the range of effective interference, the rated and maximum rotational speed are combined with different interference, and the influence of interference on the rotor strength is analyzed. As shown in Figure 12, when the interference amount is between 10 and 40 μm, the maximum principal stress at a low speed of 60,000 rpm shows a steady upward trend. However, when the speed is >88,000 rpm, the influence of the interference amount on the stress is not obvious. When the interference amount is greater than 40 μm, the maximum principal stress increases linearly with the increase in the interference amount. The specific simulation data points are shown in Table 3.

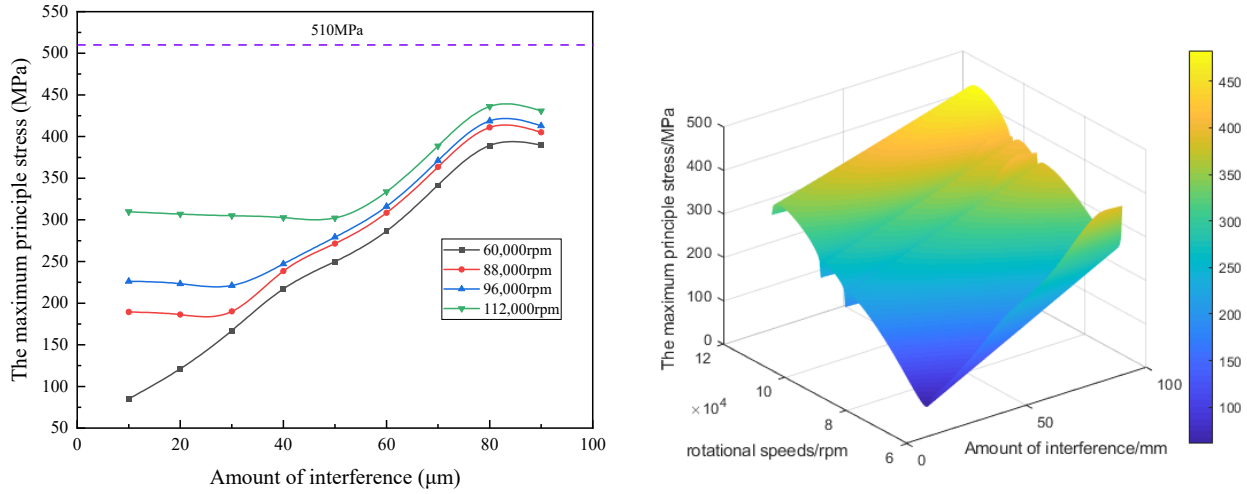


Figure 12. The relationship between the interference and stress at different rotational speeds. (**a**) 2D plane curve; (**b**) 3D Surface Plot.

Table 3. The simulation results of stress under different interference fit.

Amount of Interference (μm)	The Maximum Principle Stress (MPa)			
	60,000 rpm	88,000 rpm	96,000 rpm	112,000 rpm
10	85.20	189.29	226.26	309.83
20	121.17	186.24	223.33	306.95
30	167.15	190.12	221.16	304.98
40	217.12	238.41	247.06	302.62
50	249.85	271.51	279.20	302.24
60	286.60	308.42	316.17	333.85
70	341.82	363.54	371.16	388.70
80	389.24	410.95	418.66	436.10
90	389.78	405.03	412.93	430.82

4.2. Rotational Speeds

When the chamfer of the end covers is C0.5 and the interference amount is 60 μm, the effect of rotor speeds on the stress of the interference fit structure is analyzed. The simulation data results are shown in Table 4. It is known that the relationship between the centripetal force and rotational speed is quadratic. In addition, the stress generated by the sheath and the magnet is the compression force among the layers, and the sum value of the compression force of each layer is equal to the centripetal force and the direction is opposite. So, the maximum principal stress is also a quadratic correlation with speeds, as shown in Figure 13. Therefore, the speeds are also one of the factors for the comprehensive consideration of the rotor interference fit strength.

Table 4. The simulation results of stress under different rotor speeds.

The Rotor Speed (rpm)	The Maximum Principle Stress (MPa)
60,000	286.6
70,000	293.44
80,000	301.34
90,000	310.29
100,000	320.3
110,000	331.36

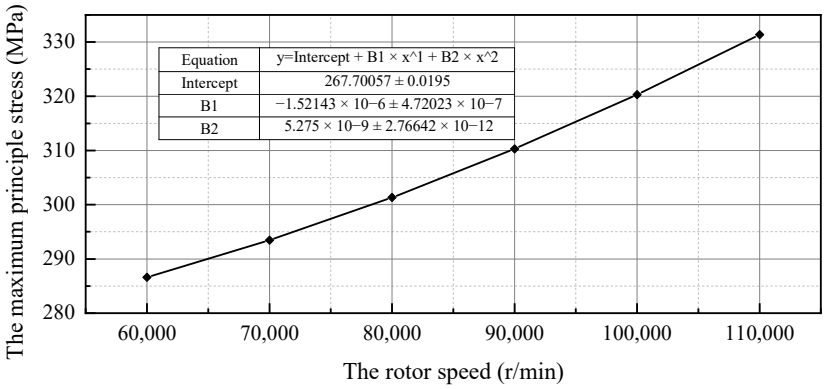


Figure 13. The stress distribution at different rotor speeds.

4.3. Temperature

When exploring the factors of rotor strength, temperature is also one of the factors that cannot be ignored. In the simulation, the temperature and stress field changes in the rotor system are mainly considered. The rotor system is regarded as an isothermal body, and the temperature load is applied to it to analyze the stress changes in the interference fit structure at different temperatures. The temperature range selected in the simulation corresponds to the actual working environment. The actual minimum operating temperature is 20 °C. On this basis, the temperature is increased to find the highest range that the system can withstand. The unit for the temperature values mentioned is Celsius.

When exploring the correlativity between temperature and stress, the coefficient of thermal expansion is an important parameter to be considered. The coefficient of the thermal expansion of the magnet, sheath, and end covers do not change obviously when the temperature ranges from 0 to 400 °C. Their coefficients of thermal expansion are approximately linear with temperature. Therefore, it is determined that the average coefficient of the thermal expansion of the magnet is $9 \times 10^{-6}/°C$, and that of the sheath and end covers is $1.7 \times 10^{-5}/°C$. The metal strength decreases when the temperature is increased. At about 250 °C, the strength of the metal increases slightly. However, the reduction in the metal strength is not obvious below 200 °C [28]. In this case, the change in the strength can be ignored.

As shown in Figure 14, the sheath is a thin-walled part where stress is affected weakly by the change in temperature. However, with the increase in temperature, the stress of the magnet and end covers increases gradually, and strength failure does not occur until up to 183.11 °C.

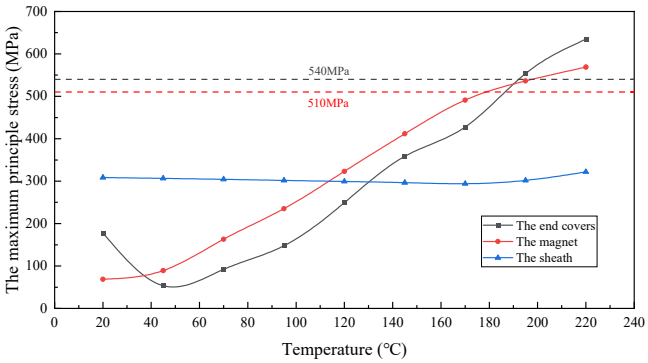


Figure 14. The stress distribution of the magnet, sheath, and end covers at different temperatures.

According to Figure 15, it can be determined where the failure occurs. The failure position of the magnet is on both end faces, while both end covers fail at the top of the small diameter sides. From the simulation results, it can be obtained that the operating temperature of the rotor system should not be too high, and it should be kept below

183.11 °C to avoid a high temperature, leading to the strength failure of the magnets and end covers.

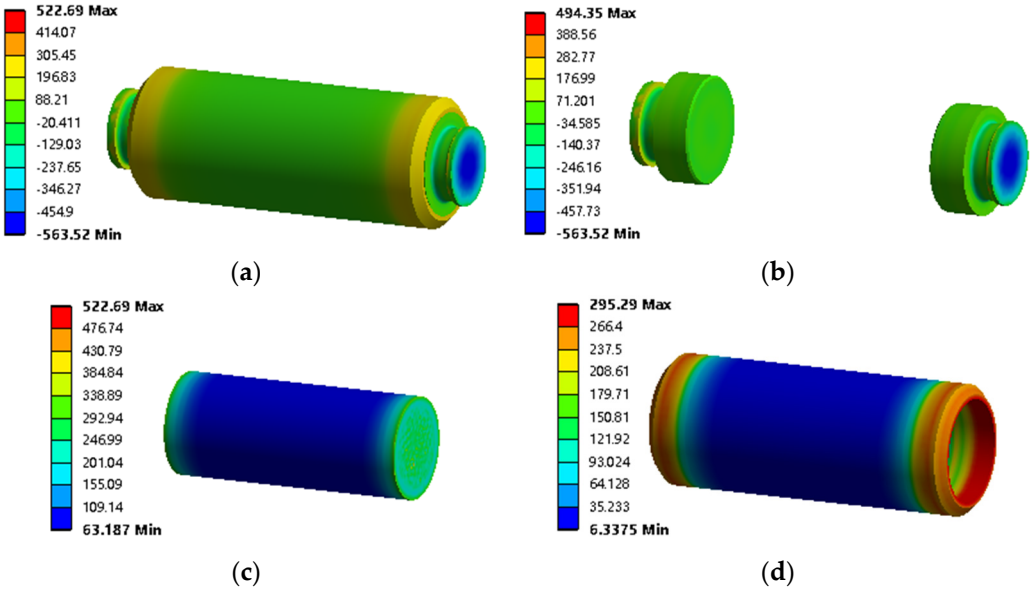


Figure 15. The stress distribution in each part at 183.11 °C. (**a**) The structure of the interference fit; (**b**) the end covers; (**c**) the magnet; (**d**) the sheath.

Compared with ordinary motors, high-speed motors have a high speed and large vibration, so the heating problem is more serious when working, which leads to the change in interference fit contact stress. In order to further understand the influence of temperature on the interference fit structure, from the point of view of strength failure, simulation is used to analyze the temperature, under which a failure problem will occur within the range of effective interference.

According to the above results, when the temperature gradient rises, the contact stress of the interference fit structure also increases. Therefore, the failure temperature point of the interference fit structure can be determined at a high working temperature. With the standard interference quantity of 60 μm and failure temperature of 183.11 °C as the reference, the temperature of the interference fit structure strength failure within the range of the effective interference quantity is further explored. A summary of the final results is shown in Figure 16. When the interference volume ranges from 20 to 70 μm, the temperature reaching the failure condition decreases step by step and reaches the inflection point, at which time the temperature is 182.3 °C. From 80 to 90 μm, the failure temperature gradually increases, and it rises to 190 °C at 90 μm. Excluding other possible influencing factors, the results are still consistent after multiple simulation verification. The possible reason is that the thermal expansion coefficient of the sheath is higher than that of the magnet, the thickness of the sheath increases, the radial stress of the structure decreases, but the interference quantity also increases, resulting in an increase in the contact stress. The stress value of the overall structure shows an upward trend before the interference value increases to 70 μm. With the accompanying effect of temperature, the failure temperature gradually decreases. But after that, the stress value of the structure gradually decreases, resulting in the rate of increase in stress slowing down as the temperature rises. This study can provide a certain reference significance for the allowable working temperature range of the rotor.

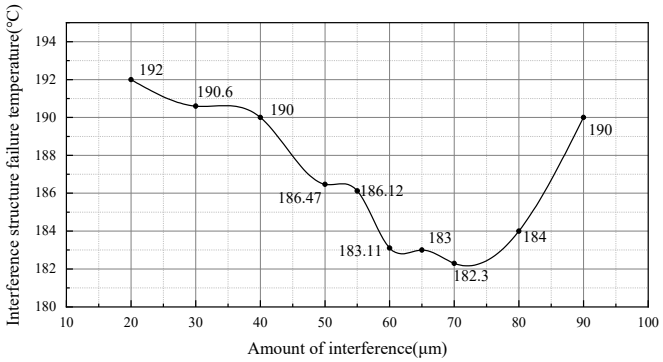


Figure 16. The relationship between the interference amount and the failure temperature of the structure.

4.4. Thicknesses of the Sheath Wall

After the chamfers are added to the end cap, the simulation results show that the maximum principal stress area of the interference fit structure changes from the end face of the magnet to the inner wall of the edge of the magnet sheath. Therefore, the influence of the sheath thickness on the interference fit structure can be studied. Based on this conclusion, the interference amount is kept at 60 μm at the rated speed of 88,000 rpm. Under the premise of no sheath damage failure, different wall thicknesses of the sheath are selected for the simulation results, and these are shown in Figure 17 below. The stress on the sheath is in the minimum range when the sheath wall thicknesses are between 4.5 and 4.75 mm.

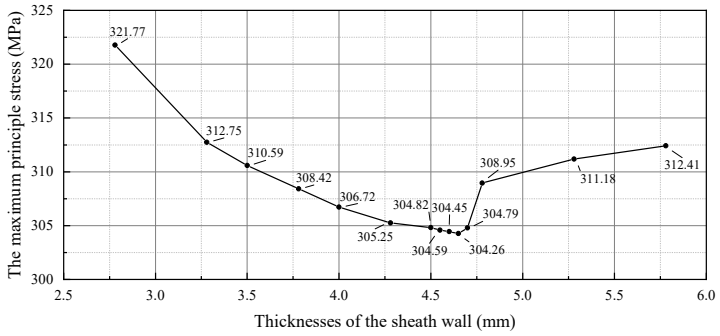


Figure 17. The stress distribution under different thicknesses of sheath wall.

As shown in Figure 18, when the sheath wall thickness is too small, the deformation resistance of the sheath is poor due to the effect of the interference fit, which causes high stress. Nevertheless, as the sheath wall thickness increases, the magnet plasticity is low and not easily deformed, so the total deformation of the sheath increases. While the sheath thicknesses are between 3 and 4.5 mm, the strain has a flat region and gradually increases thereafter. Until the sheath wall thicknesses are higher than 4.5 mm, the stress and strain generated by the sheath gradually increase. This improves the pre-stress of the sheath on the magnet. In the interference fit of the rotor, the priority of magnet protection is higher than that of sheath. However, too much thickness can lead to assembly difficulties and heat dissipation problems. Therefore, the thickness of the sheath should be determined according to the actual situation to achieve the best effect.

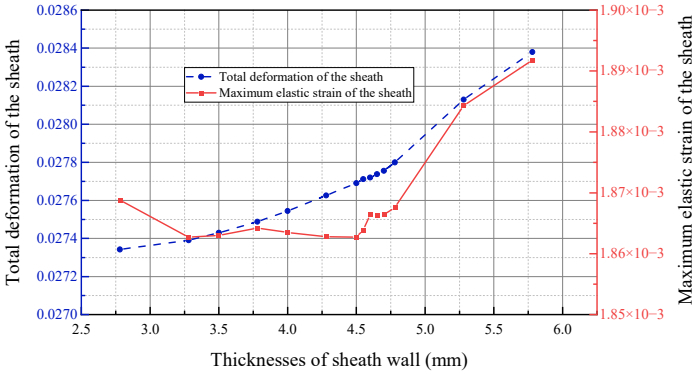


Figure 18. The total deformation and strain distribution under different thicknesses of sheath wall.

5. Conclusions

In this paper, the main influencing factors of the interference fit structure of a high-speed permanent magnet motor are analyzed, and the problem of the thermal failure of the rotor system is systematically studied. The results and research significance are as follows:

(1) A design method to reduce the edge stress concentration of the interference fit structure is proposed. The problem of stress concentration is improved by adding chamfer to the end covers of the interference fit structure. Through adding chamfers to the end covers, the maximum stress of the structure is reduced from 1186.1 MPa to 308.42 MPa, which effectively reduces the stress of the structure. This could provide a basis for the design of the structure.

(2) The reliability of the interference fit structure decreases as the amount of interference increases in the range of effective interference. When the rotational speed reaches 136,000 rpm, the structure will suffer loose speed and fail. In the actual working situation, when the speed of the high-speed permanent magnet motor approaches the critical speed, it is necessary to pay attention to the operation of the motor, and the speed cannot exceed the limit to avoid rotor structural failure and safety accidents.

The wall thickness of the sheath should be appropriate to achieve sufficient preload while the interference fit structure meets the strength requirements and plays a role in protecting the magnet. To ensure the reliability of the rotor system strength, the operation of a high-speed permanent magnet motor can be stable.

(3) The rise in temperature in the rotor system has a small effect on the stress of the sheath, but the stress on the magnet and end covers increases with the rise in temperature. According to the simulation results, it can be seen that when the temperature reaches 183.11 °C at 60 μm, the strength of the structure fails. Considering the safety, the failure temperature of the interference fit structure at different interference values is analyzed. The results show that the operating temperature of the rotor system should not exceed 180 °C as far as possible in practice. In necessary cases, heat dissipation measures for high-speed permanent magnet motors, such as air-cooling of the rotor and water-cooling of the external shell to indirectly reduce the operating temperature of the rotor, so as to ensure the reliability and safety of the system during operation.

It is necessary to acknowledge the limitations of this study. In the simulation, some minor influencing factors are normalized. In the actual working environment, the factors affecting the operation of a high-speed permanent magnet motor are not limited to the discussion in this paper. The findings in this study can provide a reference for designing the rotor structure of a high-speed permanent magnet motor, and a future study with a larger cohort size is needed to test the specific parameter requirements in practice.

Author Contributions: Conceptualization: Y.Z.; methodology: Y.Z. and S.Y.; software: Y.Z., Q.W. and J.H.; validation: Y.Z., X.Y., Q.W. and W.H.; formal analysis: S.Y.; investigation: Y.Z.; resources: Y.Z. and X.Y.; data curation: Y.Z.; writing—original draft preparation: Y.Z.; writing—review and editing:

Y.Z. and S.Y.; visualization: Y.Z.; supervision: L.Z.; All authors have read and agreed to the published version of the manuscript.

Funding: This research was funded by Research and development of air bearing centrifugal compressor for hydrogen energy vehicles, grant number K4040121332. And the APC was funded by Northwest A&F University.

Data Availability Statement: Data available on request due to restrictions eg privacy or ethical. The data presented in this study are available on request from the corresponding author. The data are not publicly available due to privacy.

Conflicts of Interest: The authors declare no conflict of interest. The funders had no role in the design of the study; in the collection, analyses, or interpretation of the data; in the writing of the manuscript; or in the decision to publish the results.

Abbreviations

d_m	Diameter of the magnet
d_s	Outer diameter of the sheath
l	Axial length of the sheath of the magnet
l_m	Axis length of the magnet
M	Maximum torque of the motor
P_{min}	Minimum binding pressure
F	Friction coefficient of mating surface
δ_{min}	Minimum interference
C_m	Stiffness coefficient of the magnet
C_s	Stiffness coefficient of the sheath
ν_m	Poisson's ratio of the magnet
v_s	Poisson's ratio of the sheath
E_m	Elastic modulus of the magnet
E_s	Elastic modulus of the sheath
σ_{sm}	Yield strength of magnet
σ_{ss}	Yield strength of sheath
q_a	Ratio of mating diameter to outer diameter of the sheath
P_{max}	Maximum pressure
δ_{max}	Maximum interference
δ_m	Radial displacement of the magnet
ρ_m	Density of the magnet
ω_m	Radial displacement of the magnet
ρ_s	Density of the sheath
δ_ω	Lost interference
Δ	Designed interference
n	Rotational speed of loosening

References

1. Zhao, F.; Yu, Z.; Cao, J.; Li, L. Design and Optimization of a High-Speed Permanent Magnet Synchronous Machine for Gas Compressors. *IEEE Trans. Magn.* **2021**, *58*, 1–5. [CrossRef]
2. Swanke, J.; Zeng, H.; Bobba, D.; Jahns, T.M.; Sarlioglu, B. Design and testing of a modular high-speed permanent-magnet machine for aerospace propulsion. In Proceedings of the 2021 IEEE International Electric Machines & Drives Conference (IEMDC), Hartford, CT, USA, 17–20 May 2021; pp. 1–8.
3. Ismagilov, F.R.; Papini, L.; Vavilov, V.E.; Gusakov, D.V. Design and Performance of a High-Speed Permanent Magnet Generator with Amorphous Alloy Magnetic Core for Aerospace Applications. *IEEE Trans. Ind. Electron.* **2019**, *67*, 1750–1758. [CrossRef]
4. Indri, M.; Bellissimo, M.; Pesce, S.; Perna, V. A Robust H∞ Application for Motor-Link Control Systems of Industrial Manipulators. *Appl. Sci.* **2022**, *12*, 8890. [CrossRef]
5. Cristea, M.; Vladutoiu, L.; Grigore, A.; Cristea, D. Types of Electric Motor Controllers That Can Be Used on Agricultural Electric Tractors. *Ann. Univ. Craiova-Agric. Mont. Cadastre Ser.* **2021**, *51*, 235–250. [CrossRef]
6. Wang, H.; Leng, J. Summary on development of permanent magnet synchronous motor. In Proceedings of the 2018 Chinese Control and Decision Conference (CCDC), Shenyang, China, 9–11 June 2018; pp. 689–693.
7. Zhou, Y.; Tian, L.; Gao, S.H.; Zhang, J.W.; Yang, L.K.; Xie, R.G. Design and testing of CFRP sleeve for a high-speed permanent magnet synchronous motor with surface-mounted rotor. *Mech. Sci. Technol.* **2021**, *35*, 221–230. [CrossRef]

8. Krykowski, K.; Gałuszkiewicz, Z.; Gałuszkiewicz, P.; Hetmańczyk, J.; Całus, D. High-speed Permanent Magnet Brushless DC Motors, properties and prospective applications. *Przegląd Elektrotechniczny* **2019**, *95*, 139–145. [CrossRef]
9. Liu, R.; Yan, C.S.; Zeng, C.; Liu, L.H. Interference Fit Design and Simulation Research for Rotor of High Speed Permanent Magnet Machine. *Small Spec. Electr. Mach.* **2020**, *48*, 17–19.
10. Shen, J.; Qin, X.; Wang, Y. High-speed permanent magnet electrical machines—Applications, key issues and challenges. *CES Trans. Electr. Mach. Syst.* **2018**, *2*, 23–33. [CrossRef]
11. Xiao, J.C.; Xiao, S.H.; Wu, H. Design and Strength Analysis of Ultra-High Speed Permanent Magnet DC Rotor. *Adv. Mater. Res.* **2011**, *188*, 481–486. [CrossRef]
12. Pu, T.; Du, G.; Tong, J.; Huang, N.; Li, N.; Xu, W. Comparison of Rotor Strength of Various Rotor Structures for Ultra-high-speed Permanent Magnet Synchronous Motor. In Proceedings of the 2021 IEEE 4th Student Conference on Electric Machines and Systems (SCEMS), Huzhou, China, 1–3 December 2021; pp. 1–6.
13. Liu, G.; Liu, M.; Zhang, Y.; Wang, H.; Gerada, C. High-speed permanent magnet synchronous motor iron loss calculation method considering multiphysics factors. *IEEE Trans. Ind. Electron.* **2019**, *67*, 5360–5368. [CrossRef]
14. Du, G.; Xu, W.; Zhu, J.; Huang, N. Effects of design parameters on the multiphysics performance of high-speed permanent magnet machines. *IEEE Trans. Ind. Electron.* **2019**, *67*, 3472–3483. [CrossRef]
15. Gan, C.; Chen, Y.; Cui, X.; Sun, J.; Ni, K.; Qu, R. Investigation of rotor strength and rotor dynamics for high-speed high-power switched reluctance machines. *IET Electr. Power Appl.* **2020**, *14*, 1624–1630. [CrossRef]
16. Xu, Y.; Ai, M.; Wang, W.; Wang, Y. Composite sheath of high-speed permanent magnet generator with rotor strength constraint. *Int. J. Appl. Electromagn. Mech.* **2019**, *61*, 247–262. [CrossRef]
17. Shao, Y.; Wang, X.; Gao, Q.; Li, Y. Rotor Strength Analysis of Ultra-High Speed Permanent Magnet synchronous Motor. In Proceedings of the 2019 22nd International Conference on Electrical Machines and Systems (ICEMS), Harbin, China, 11–14 August 2019.
18. Zheng, M.; Huang, W.; Gao, C. Rotor stress and dynamics analysis of a high-speed permanent magnet machine for a micro gas turbine considering multiphysics factors. *IEEE Access* **2020**, *8*, 152523–152531. [CrossRef]
19. Zheng, L.; Yue, F.H.; Wang, L.Y.; Liu, H.X.; Wang, Q.J. Electromagnetic-thermal-stress Coupling Analysis of the Ironless Permanent Magnet Synchronous Linear Motor. *Micromotors* **2019**, *52*, 1–6.
20. Ying-Ga, W.U.; Chen, G.D.; Wang, Y.J. Research on Motor Temperature Rise of Aeroengine Rotor Test System. *Aeroengine* **2019**, *45*, 47–52.
21. Chen, L.; Zhu, C. Rotor strength analysis for high speed permanent magnet machines. In Proceedings of the 2014 17th International Conference on Electrical Machines and Systems (ICEMS), Hangzhou, China, 22–25 October 2014; pp. 65–69.
22. Du, G.; Xu, W.; Zhu, J.; Huang, N. Rotor stress analysis for high-speed permanent magnet machines considering assembly gap and temperature gradient. *IEEE Trans. Energy Convers.* **2019**, *34*, 2276–2285. [CrossRef]
23. Du, G.; Huang, N.; Zhao, Y.; Lei, G.; Zhu, J. Comprehensive sensitivity analysis and multiphysics optimization of the rotor for a high speed permanent magnet machine. *IEEE Trans. Energy Convers.* **2020**, *36*, 358–367. [CrossRef]
24. Gu, Y.; Wang, X.; Gao, P.; Li, X. Mechanical analysis with thermal effects for high-speed permanent-magnet synchronous machines. *IEEE Trans. Ind. Appl.* **2021**, *57*, 4646–4656. [CrossRef]
25. Xu, P.; Lv, X.B.; Hu, J.Q.; Li, B.; Yang, Y.F. Simulation Research on Interference Fit and Structural Improvement of Planetary Shelf Components Based on Ansys Workbench. *Lift. Transp. Mach.* **2020**, *14*, 32–38.
26. Lu, W.K.; Zhang, W.; Ge, F.H.; Zhang, D.P. Static and modal analysis of high-speed permanent-magnet motor rotor. *Mod. Mach.* **2018**, *5*, 46–49.
27. Wei, Y.G.; Song, Y.X.; Li, J.; Dong, S.J. Interference Fit Contact Edge Effect and Stress Concentration. *J. Dalian Railw. Inst.* **2003**, *3*, 4–8.
28. Sun, J.; Nitschke-Pagel, T.; Dilger, K. Influence of temperature- and phase-dependent yield strength on residual stresses in ultra-high strength steel S960 weldments. *J. Mater. Res. Technol.* **2021**, *15*, 1854–1872. [CrossRef]

Disclaimer/Publisher's Note: The statements, opinions and data contained in all publications are solely those of the individual author(s) and contributor(s) and not of MDPI and/or the editor(s). MDPI and/or the editor(s) disclaim responsibility for any injury to people or property resulting from any ideas, methods, instructions or products referred to in the content.